Luminescent Compounds *fac*- and *mer*-Aluminum Tris(quinolin-8-olate). A Pure and Hybrid Density Functional Theory and Time-Dependent Density Functional Theory Investigation of Their Electronic and Spectroscopic Properties

Mario Amati and Francesco Lelj*

La.MI Dipartimento di Chimica and LaSCAMM, INSTM Sezione Basilicata, Università della Basilicata, Via Nazario Sauro 85-85100 Potenza, Italy

Received: September 12, 2002; In Final Form: November 29, 2002

Density functional theory and time-dependent density functional theory have been applied to describe the ground and excited states and the spectral characteristics of the meridianal and facial isomers of aluminum tris(quinolin-8-olate) (Alq_3). Vertical absorption wavelengths and oscillator strengths of both meridianal Alq_3 and facial Alq_3 have been computed up to about 255 nm (4.86 eV) and compared with experimental data. Experimental meridianal Alq_3 absorption band locations are well reproduced by the computations, allowing easy assignment of the absorption bands. The facial Alq_3 absorption spectrum has been computed, and a detailed comparison of the excited state characteristics of the two isomers has been addressed for pointing out differences in absorption and emission properties. This work suggests that the facial Alq_3 may be the constituent of the recently reported Alq_3 crystalline phase known as the δ-phase. This is an important new material for understanding the Alq_3 solid-state properties and for a possible organic light-emitting diode fabrication. Some suggestions to experimentally distinguish the two isomers have been presented. Furthermore, information about the excited-state kinetics of both the isomers and properties of their emissive excited states has been gained. Both the hybrid B3LYP and the pure BLYP, LSDA, BPW91, and LB94 exchange-correlation functionals have been tested, and the B3LYP functional clearly seems to be the best choice for this class of molecules.

Introduction

LED (light-emitting diode) technology is causing deep changes in lighting applications. As reported in a recent paper,[1] "in comparison to incandescent bulbs, LEDs are smaller, longer lived, more energy efficient, more robust, less heat generating, more directional and they have faster switching...". Given their characteristics, it is easy to predict that they will replace traditional lighting devices with consequent reduced environmental impact and generally improved performances.

In this regard, the use of organic compounds as constituents of organic LEDs (OLEDs) promises additionally improved capabilities. In particular, LEDs based on low-molecular-weight organic compounds represent an emerging technology. Among them, aluminum tris(quinolin-8-olate) (Alq_3; Figure 1) is one of the most studied electroluminescent substances by virtue of its relative stability, electron transport, and emitting properties together with easy wide-area deposition and low-cost purification. Its characteristics well describe the additional benefits deriving from the utilization of organic compounds, such as low production costs, increased flexibility, and improved energy efficiency.

In these diodes, Alq_3 constitutes thin amorphous films whose nature is the object of multiple recent theoretical and experimental works. The existence of two Alq_3 isomers, the "meridianal" and "facial" shown in Figure 2 (*mer*-Alq_3 and *fac*-Alq_3 in the following), is the object of debate about film composition. On the basis of ab initio theoretical investigations, Curioni et al. has suggested that the coexistence of the two isomers in thin films may be a cause of its amorphous character.[2] According to their computations, *fac*-Alq_3 is less stable in energy than *mer*-Alq_3, but shows a greater dipole moment which could act as a stabilizing factor in the condensed phase. The greater stability of *mer*-Alq_3 agrees with previously reported X-ray studies of solvated Alq_3 crystals which showed only *mer*-Alq_3.[3,4] Additionally, solution proton NMR studies allowed the observation of only *mer*-Alq_3.[5] Only recently, not-solvated Alq_3 crystal

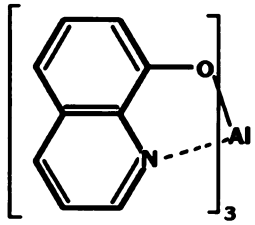

Figure 1. Alq_3, aluminum tris(quinolin-8-olate).

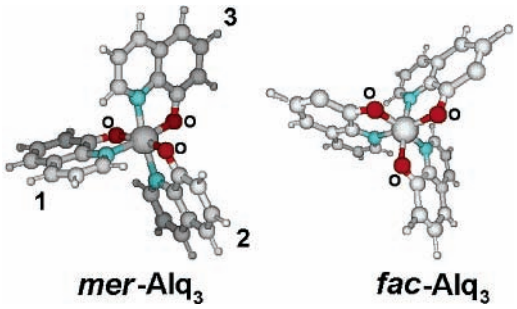

Figure 2. Meridianal and facial isomers of Alq_3. The chelants in *mer*-Alq_3 are labeled with numbers 1−3.

* To whom correspondence should be addressed. E-mail: lelj@unibas.it.

10.1021/jp026981e CCC: $25.00
Published on Web 03/18/2003

characterization has been reported.[6] Two different pure Alq_3 crystalline phases, called α- and β-phases, were demonstrated to be certainly constituted by *mer*-Alq_3, but in the third described crystalline phase, called the γ-phase, the presence of *fac*-Alq_3 could not be definitely excluded. However, the newly observed *mer*-Alq_3 crystal polymorphism was considered a possible origin of the amorphous character in condensed phases, to be added to local fluctuations in enantiomeric concentration during deposition. Therefore, interconversion between *mer*- and *fac*-Alq_3 during sublimation and their contemporary deposition did not appear a necessary condition for obtaining amorphous films.

More recently, a new crystal attributed to *fac*-Alq_3 has been reported.[7] It differs from the previously studied crystals by a blue-shifted fluorescence band, a blue-shifted excitation edge in photoluminescence absorption spectra, a simpler Raman IR spectrum (suggesting the higher symmetry of *fac*-Alq_3), and a much lower triplet-state population during fluorescence. Furthermore, thermal sublimation between 330 and 370 °C produced a fraction principally constituted by α-phase *mer*-Alq_3 with inclusion of the δ-phase. Unfortunately, a clear assignment of atomic positions within the unit cell has not been possible due to the small dimensions of the produced crystals, and thus, *fac*-Alq_3 has not been clearly identified.

Confirming the existence of distinct *mer*-Alq_3 and *fac*-Alq_3 crystals can be a fundamental progress to definitively establish the composition of amorphous films. Moreover, it can represent a significant improvement in our knowledge of Alq_3 solid-phase properties, with clear advantages in technological applications. For example, comparative studies of *mer*- and *fac*-Alq_3 crystals can lead to the design of valid analytical methods for distinguishing and quantifying the two isomers. This would allow the relation of the condensed-phase composition to its preparation techniques and conditions, or could lead to a tuning of the Alq_3 thin-film properties varying their composition. Alternatively, the same comparative studies could lead to the definitive exclusion of the *fac*-Alq_3 presence in amorphous films.

These are only a few examples of the new research fields and knowledge which could derive from the comparison between the two isomers.

In this respect, theoretical investigations can represent an important contribution. Comparison of the computed spectral characteristics between the two isomers can be an additional confirmation of the presence of *fac*-Alq_3 in δ-phase crystals. Moreover, it could be a valuable tool for microscopic interpretations of *mer*-Alq_3 known properties, probably better than calculations involving only one isomer. In fact, computed differences in molecular properties are expected to be in better agreement with their experimental counterparts.

The calculations reported in this paper concern the determination of the vertical excitation energies from the ground state, the corresponding oscillator strengths, and excited-state composition. The comparison among different xc (exchange-correlation) functionals has allowed the selection of the best choice for this class of compounds. This has been achieved by matching the lowest energy part of *mer*-Alq_3 computed spectra with the first broad experimental absorption band. Afterward, absorption spectra have been computed up to about 255 nm for both *mer*- and *fac*-Alq_3, allowing assignments of observed absorption bands. Computation of the spectrum up to relatively high energy transitions (4.93 eV) represented a further test of the used functional. Transitions in the UV−vis range and characteristics of excited states have been compared in the case of the two isomers. This comparative study has been useful also for a deeper understanding of known properties of *mer*-Alq_3.

Computational Details

Molecular geometries were optimized using the Kohn−Sham density functional theory (DFT) with the 3-21G(d) and 6-31G(d) basis sets and the Becke three-parameter hybrid exchange-correlation functional known as B3LYP.[8] Analytical evaluation of the energy second-derivative matrix with respect to Cartesian coordinates (Hessian matrix) at the same level of approximation confirmed the nature of minima of the potential energy surface stationary points associated with the optimized structures.

Time-dependent density functional theory (TD-DFT)[9,10] allowed the computation of excitation energies, oscillator strengths, and excited-state compositions in terms of excitations between occupied and virtual orbitals. TD-DFT calculations were performed using the following exchange-correlation functionals: B3LYP,[8] BLYP (Becke's 1988 exchange[11] and correlation of Lee, Yang, and Parr[12]), BPW91 (Becke's 1988 exchange[11] and 1991 correlation of Perdew and Wang[13]), LSDA (the pure-exchange electron gas formula with $\rho^{4/3}$ and a coefficient of 2/3 and 1980 correlation functional of Vosko, Wilk, and Nusair[14]), and LB94 (exchange correlation of Van Leeuwen and Baerends[15]). All these computations were performed on the B3LYP/6-31G(d) geometries.

Geometry optimizations and all the TD-DFT calculations excluding the LB94 computations were performed using the Gaussian 98[16] suite of programs. TD-DFT computations were done using the 6-31G(d) contracted Gaussian basis set.

The TD-DFT results of the LB94 functional were achieved by the ADF2000[17] program using the double-ζ STO basis set plus one polarization function on each atom (ADF set III).[18]

Figures 2 and 4 have been produced by the program Molden3.7.[19]

Results

1. *mer*-Alq_3 and *fac*-Alq_3. Geometry and Electronic Structure. *fac*-Alq_3 is characterized by three oxygen atoms and three nitrogen atoms on opposite faces of the octahedron, with consequent C_3 maximum point group symmetry. The geometry has been optimized at the B3LYP/3-21G(d) and B3LYP/6-31G(d) levels of approximation, both with and without C_3 point group symmetry constraints. Vibrational analysis at the same level of approximation confirmed that the ground-state geometry belongs to the C_3 point group.

mer-Alq_3 is necessarily asymmetric (C_1 point group). Its geometry has been optimized at the B3LYP/6-31G(d) level. Given its asymmetric character, the three chelants can be distinguished and have been labeled with the numbers 1−3 (Figure 2).

Some geometrical parameters of the *mer*-Alq_3 and *fac*-Alq_3 coordination sphere are collected in Table 1 and compared with similar data from previously published theoretical[2,20] and experimental[3,4,6] works. Tables 1S and 2S in the Supporting Information contain the complete geometries of both isomers computed at the B3LYP/3-21G(d) and B3LYP/6-31G(d) levels. According to both computational and experimental results for *mer*-Alq_3, the longest Al−N bond distance involves the unique nitrogen atom opposite the oxygen atom (Al−N1), while the remaining two Al−N distances show smaller values. Not surprisingly, this longer Al−N bond distance is opposite the shortest of the Al−O bond distances (Al−O3), whereas the other two Al−O bond distances show larger and more similar values. In the case of the *fac*-Alq_3 structure, where three oxygen atoms are opposite nitrogen atoms, Al−O and Al−N distances are close to Al−O3 and Al−N1 *mer*-Alq_3 distances, respectively.

TABLE 1: Selected Bond Lengths (Å), Dipole Moments (D), and Zero-Point Energies (kcal/mol) Computed for *mer*-Alq_3 and *fac*-Alq_3[a]

		B3LYP/6-31G(d)[b]	BLYP[c]	HF/3-21+G** [d]	exptl[e]	exptl[f]	exptl[g]
mer-Alq_3	Al−O1	1.881	1.880	1.856	1.850	1.863	1.860
	Al−O2	1.884	1.885	1.866	1.880	1.858	1.857
	Al−O3	1.855	1.860	1.826	1.841	1.849	1.850
	Al−N1	2.125	2.151	2.117	2.074	2.078	2.087
	Al−N2	2.064	2.073	2.033	2.026	2.033	2.017
	Al−N3	2.084	2.089	2.063	2.048	2.035	2.050
	m	4.41	4.1	5.51			
fac-Alq_3	Al−O	1.851	1.852				
	Al−N	2.135	2.147				
	m	7.9	7.1				
	ΔE_0(*fac*−*mer*)	4.9	4.0				

[a] Experimental data are included for comparison. [b] This paper. [c] Plane-wave basis set up to the energy cutoff of 70 Ry (Curioni et al., ref 2). [d] Shelegel et al., ref 20. [e] Crystal containing methanol, ref 3. [f] Crystal containing acetyl acetate, ref 4. [g] Pure *mer*-Alq_3 crystal, ref 6.

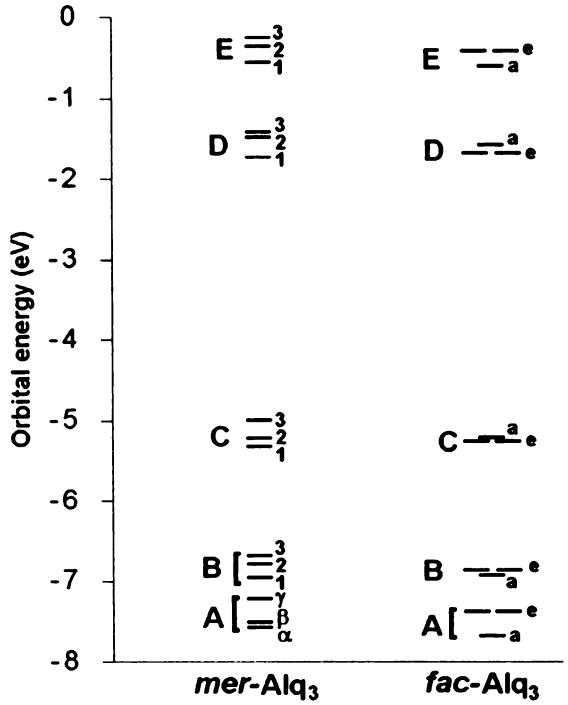

Figure 3. Scheme of the molecular orbital energy levels close to the HOMO and LUMO computed at the B3LYP/6-31G(d) level of approximation for *mer*-Alq_3 and *fac*-Alq_3. See Tables 2 and 3 for the exact values of the one-particle orbital energies.

mer-Alq_3 seems more stable in energy than *fac*-Alq_3. At the B3LYP/6-31G(d) level, the difference in electronic energy amounts to 5.0 kcal/mol. Inclusion of zero-point energy contributions reduces this difference to 4.9 kcal/mol. These values match well with the 4.4 kcal/mol results of the BLYP computations reported in Table 1, but strongly differ from the 7.8 kcal/mol (not reported in Table 1) obtained using the same xc potential (B3LYP) and SDD effective core potential.[21] As reported in Table 1, the dipole moment is much greater in *fac*-Alq_3.

Figure 3 shows the molecular orbital (MO) energy levels close to the highest occupied molecular orbital (HOMO) of *mer*-Alq_3 and *fac*-Alq_3 computed at the B3LYP/6-31G(d) level of approximation. The levels are gathered in sets of three close-spaced orbitals, labeled with letters from A to E. Sets A−C MOs are occupied, and sets D and E MOs are virtual. Tables 2 and 3 collect information about the MOs such as one-electron energy and composition in terms of fragment orbitals. From the listed values, all the MOs are substantially localized on one or more chelants, with only small contributions from aluminum atomic orbitals. Furthermore, it is possible to distinguish one type of fragment orbital as the principal constituent of each MO in each set. The fragment orbitals are shown in Figure 4, where the correspondence between MO sets and fragment orbitals is stressed by labeling the fragment orbitals with the same capital letter identifying the associated set.

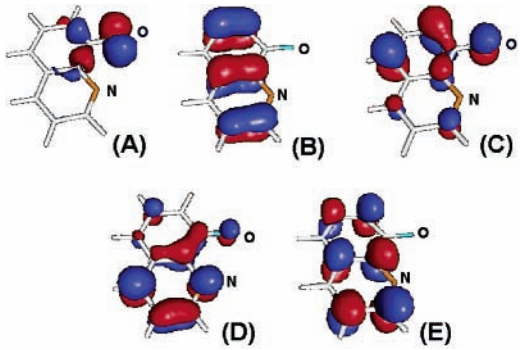

Figure 4. Chelant fragment orbitals mainly involved in the generation of the molecular orbitals of sets A−E (Figures 2 and 3). The letter in parentheses identifies the set.

All the mentioned findings are common to both isomers. However, they differ in how the orbitals are distributed among chelants.

In *mer*-Alq_3, sets B−E MOs are mainly localized on a single chelant, as inferred from the percentage composition in terms of fragment orbitals reported in Table 2. For this reason, each orbital of the set can be assigned to a single chelant and identified with the numeric label associated with the chelant as in Figure 2. It is interesting to note that the lowest energy level in each set is associated with chelant 1, while the highest one is associated with chelant 3. For this reason the HOMO is localized on chelant 3, while the LUMO is localized on chelant 1. Set A MOs are more delocalized on the three chelants, so that it is impossible to clearly assign them to a single chelant. Accordingly, these MOs are labeled by letters α, β, and γ. The origin of this difference between set A MOs and the other MOs is associated with the greater interaction between A-type fragment orbitals (Figure 4) and those of the aluminum atom. This is indicated by the larger percent weight of aluminum in these MOs (Tables 2 and 3). A direct explanation of this effect can be found in the σ-type nature of the A-type fragment orbitals (the other fragment orbitals are π), together with the great weight that the donor oxygen atom assumes in the same fragment orbital (Figure 4).

In *fac*-Alq_3, each group contains a totally symmetric orbital and two degenerate orbitals, labeled with the irreducible representation symbols "a" and "e". The orbitals are necessarily

TABLE 2: One-Electron Energies and Percentage Composition of the Highest Occupied and the Lowest Unoccupied MOs in Terms of the Aluminum Atom and the Three Quinolin-8-olate Fragments for *mer*-Alq_3[a]

orbital	energy (eV)	MO composition in terms of fragments (%)	MO composition (%) (threshold 10%)
A-α	**−7.59**	Al: 5.3 chelant 1: 18.8 chelant 2: 48.6 chelant 3: 27.4	orbital A (chelant 1): 13.9 orbital A (chelant 2): 37.8 orbital A (chelant 3): 12.4
A-β	**−7.52**	Al: 4.8 chelant 1: 56.0 chelant 2: 10.9 chelant 3: 28.3	orbital A (chelant 1): 49.4 orbital A (chelant 2): 19.1
A-γ	**−7.22**	Al: 5.0 chelant 1: 14.3 chelant 2: 30.6 chelant 3: 50.0	orbital A (chelant 1): 11.5 orbital A (chelant 2): 27.8 orbital A (chelant 3): 43.3
B-1	**−6.96**	Al: 0.0 chelant 1: 98.4 chelant 2: 0.8 chelant 3: 0.8	orbital B (chelant 1): 98.0
B-2	**−6.80**	Al: 0.0 chelant 1: 0.7 chelant 2: 98.9 chelant 3: 0.4	orbital B (chelant 2): 98.5
B-3	**−6.70**	Al: 0.0 chelant 1: 0.8 chelant 2: 0.3 chelant 3: 98.9	orbital B (chelant 3): 98.6
C-1	**−5.33**	Al: 0.7 chelant 1: 96.3 chelant 2: 1.7 chelant 3: 1.3	orbital C (chelant 1): 85.9
C-2	**−5.22**	Al: 0.9 chelant 1: 2.1 chelant 2: 85.4 chelant 3: 11.7	orbital C (chelant 2): 74.7
C-3 (HOMO)	**−5.00**	Al: 0.6 chelant 1: 0.5 chelant 2: 12.2 chelant 3: 86.7	orbital C (chelant 2): 11.3 orbital C (chelant 3): 78.4
D-1 (LUMO)	**−1.73**	Al: 0.8 chelant 1: 83.3 chelant 2: 15.3 chelant 3: 0.6	orbital D (chelant 1): 78.8 orbital D (chelant 2): 13.9
D-2	**−1.50**	Al: 0.7 chelant 1: 9.7 chelant 2: 62.6 chelant 3: 27.0	orbital D (chelant 2): 59.2 orbital D (chelant 3): 25.2
D-3	**−1.42**	Al: 0.5 chelant 1: 6.5 chelant 2: 21.4 chelant 3: 71.7	orbital D (chelant 2): 20.5 orbital D (chelant 3): 68.5
E-1	**−0.56**	Al: 0.1 chelant 1: 92.0 chelant 2: 3.2 chelant 3: 4.7	orbital E (chelant 1): 91.7
E-2	**−0.36**	Al: 0.1 chelant 1: 2.2 chelant 2: 95.3 chelant 3: 2.4	orbital E (chelant 2): 94.9
E-3	**−0.26**	Al: 0.1 chelant 1: 5.7 chelant 2: 1.4 chelant 3: 92.8	orbital E (chelant 3): 92.4

[a] The largest fragment-orbital contributions are reported (threshold 10%). The fragment orbitals are shown in Figure 4, and the energy trend of their levels is reported in Figure 3.

delocalized on the three chelants, and will be identified by the capital letter of the set (A−E) and the small letter "a" or "e". The HOMO belongs to the totally symmetric irreducible representation and has an energy value close to that of the degenerate HOMO − 1. The LUMO is a degenerate orbital as well.

TABLE 3: One-Electron Energies and Percentage Composition of the Highest Occupied and the Lowest Unoccupied MOs in Terms of the Aluminum Atom and the Three Symmetry-Related Quinolin-8-olate Fragments for *fac*-Alq_3[a]

orbital	energy (eV)	composition in terms of fragments (%)	MO composition (%) (threshold 10%)
A-a	**−7.68**	Al: 5.4 chelants: 94.6	orbital A: 76.4
A-e	**−7.38**	Al: 5.1 chelants: 94.9	orbital A: 77.1
B-a	**−6.94**	Al: 0.0 chelants: 100.0	orbital B: 99.0
B-e	**−6.97**	Al: 0.0 chelants: 100.0	orbital B: 99.4
C-e	**−5.22**	Al: 0.9 chelants: 99.1	orbital C: 87.8
C-a (HOMO)	**−5.20**	Al: 0.8 chelants: 99.2	orbital C: 88.9
D-e (LUMO)	**−1.68**	Al: 0.6 chelants: 99.4	orbital D: 93.2
D-a	**−1.58**	Al: 0.5 chelants: 99.5	orbital D: 95.9
E-a	**−0.62**	Al: 0.1 chelants: 99.9	orbital A: 99.1
E-e	**−0.42**	Al: 0.1 chelants: 99.9	orbital E: 99.1

[a] The largest fragment-orbital contributions are reported (threshold 10%). The fragment orbitals are shown in Figure 4, and the energy trend of their levels is graphically reported in Figure 3.

From the values listed in Tables 2 and 3, a certain similarity between the two isomers in the one-electron energies of occupied and virtual MOs is evident. However, the HOMO−LUMO gap is 3.27 and 3.52 eV in *mer*-Alq_3 and *fac*-Alq_3, respectively, a fact that could affect the absorption and emission features of the two isomers.

As mentioned above, the energy difference between the HOMO and the HOMO − 1 in *fac*-Alq_3 is only 0.07 eV.

2. Comparison between the Exchange-Correlation Functionals. Figure 5 shows the *mer*-Alq_3 energy level scheme computed using different xc functionals on the same B3LYP/6-31G(d) geometry. The *mer*-Alq_3 B3LYP/6-31G(d) energy levels of Figure 3 are included for comparison. As in the case of the B3LYP functional, the pure functional MOs can be divided into five sets (from A to E) according to the fragment orbital from which they mainly originate. Unlike the B3LYP functional, all the pure functionals show more similar sets A and B MO energies. On the other hand, energies of sets from B to E follow the same sequence as the B3LYP functional. Moreover, the energy sequence of chelant-localized orbitals from 1 to 3 is preserved in each set.

BLYP-DFT computations using a plane-wave basis set[2] reported the same sequence of MOs as found by us for sets C−E. HF/3-21G* calculations[20] also produce the same trend for the HOMO and LUMO, but in this case the LUMO + 1 is mainly localized on chelant 3 rather than on chelant 2. Apart from this disagreement, it is likely that the origin of the level scheme pattern can be related to geometrical characteristics such as chelant deformation and, probably to a larger extent, to chelant−metal interaction rather than to artifacts due to the particular xc functional or basis set. This consideration gains importance taking into account the good agreement between computed and experimental trends of geometrical parameters (Table 1).

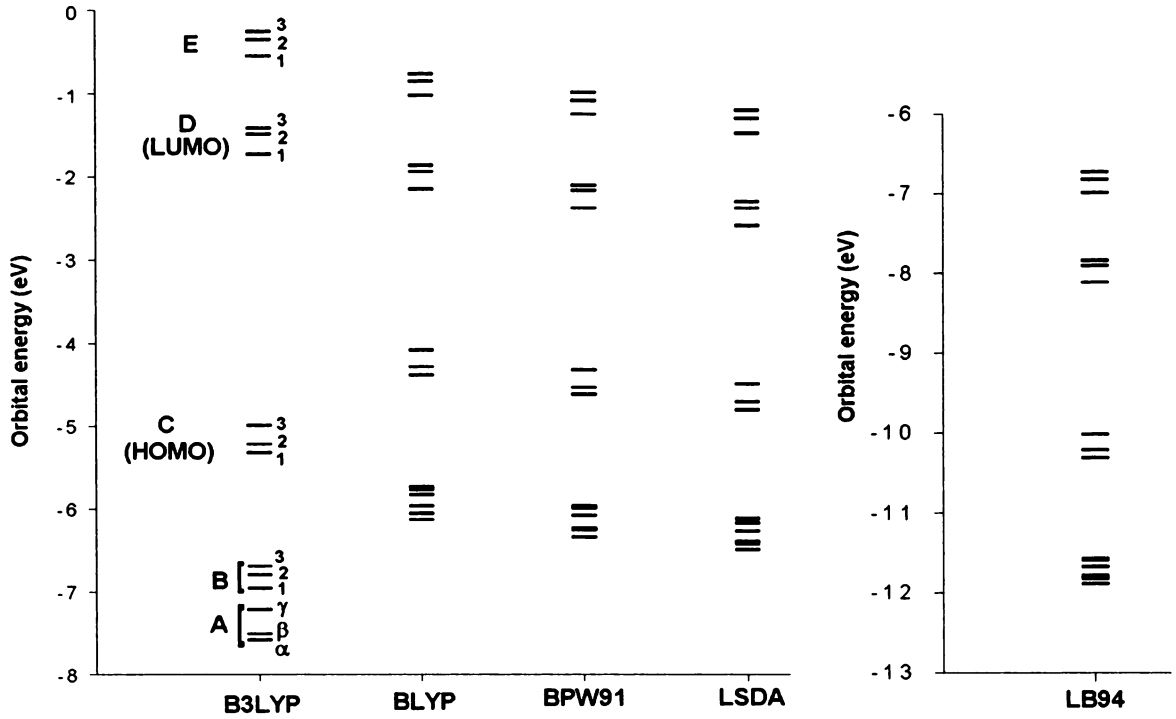

Figure 5. *mer*-Alq_3 molecular orbital energy scheme computed by different exchange-correlation functionals.

TABLE 4: HOMO−LUMO Gaps and Ionization Thresholds (the Negative of the HOMO One-Electron Energy) Computed at Different Levels of Approximation for *mer*-Alq_3

	B3LYP/6-31G(d)	BLYP/6-31G(d)	BPW91/6-31G(d)	LSDA/6-31G(d)	LB94 ADF set III
HOMO−LUMO gap (eV)	3.27	1.93	1.94	1.91	1.91
ionization threshold (eV)	5.00	4.09	4.33	4.51	10.02

TABLE 5: The First Four Singlet−Singlet Excitation Energies (nm) and Oscillator Strengths (in Parentheses) Computed by Different Exchange-Correlation Functionals for *mer*-Alq_3

excitation	B3LYP/6-31G(d)	BLYP/6-31G(d)	BPW91/6-31G(d)	LSDA/6-31G(d)	LB94 ADF set III	exptl[a]
1	447 (0.0052)	639 (0.0009)	637 (0.0009)	645 (0.0009)	649 (0.0084)	373−410
2	427 (0.0671)	576 (0.0005)	574 (0.0006)	580 (0.0006)	587 (0.0038)	
3	422 (0.0021)	565 (0.0087)	563 (0.0090)	568 (0.0090)	576 (0.0768)	
4	417 (0.0424)	527 (0.0138)	525 (0.0143)	529 (0.0140)	539 (0.0112)	

[a] Range derived from experimental work on *mer*-Alq_3 solutions, crystals, and amorphous phases (refs 6 and 22).

From Figure 5 it is evident that the B3LYP functional produces significant larger energy gaps between occupied and virtual orbitals. As reported in Table 4, the HOMO−LUMO gap of the B3LYP functional is almost twice as large as the other functionals. This finding may be associated with the contribution of the Hartree−Fock (HF) exchange in the B3LYP functional.[8] In fact, the HOMO−LUMO gap computed at the HF/6-31G(d) level of approximation on the same geometry amounts to 5.25 eV (this value is not reported in Table 4 and Figure 5). Thus, the B3LYP/6-31G(d) HOMO−LUMO gap (3.25 eV) represents an intermediate value between the HF/6-31G(d) value and the pure xc functional value (1.92 eV on average). The ionization threshold (the negative of the HOMO one-electron energy) is somewhat larger in the B3LYP calculation in comparison to the pure functionals apart from the LB94 functional, which normally produces overestimated ionization thresholds by virtue of its different asymptotic behavior.[15] The vertical ionization potential, roughly estimated by the ionization threshold, has been reported at 7.33 eV in the gas phase and 6.35 eV in Alq_3 thin films.[22]

The differences between the HOMO−LUMO gaps of B3LYP and the other functionals can be closely related to the excitation energies computed using the TD-DFT. As shown in Table 4, all the pure functionals predict significantly red-shifted first excitation energies in comparison to the B3LYP functional. The first transition with oscillator strength greater than 0.010 is predicted in the range from 525 to 576 nm, whereas the first relevant transition is computed at 427 nm by the B3LYP functional. The *mer*-Alq_3 experimental lowest energy absorption is placed between 373 and 383 nm for Alq_3 in solution,[6,23] and between 390 and 410 nm in the solid phase.[6] Amorphous films present the first band at 390 nm for film thicknesses of both 50 nm[6] and 840 nm.[24] In Table 5 an experimental range of values (373−410 nm) is reported for comparison with the computed lowest excitation energies. It is evident that the B3LYP functional is the best performer among the tested ones; therefore, it has been chosen to calculate excitation energies and oscillator strengths up to about 250 nm for both *mer*-Alq_3 and *fac*-Alq_3.

3. Absorption Features of *mer*-Alq_3. With the aim of assigning the *mer*-Alq_3 absorption bands, the experimental spectrum of Alq_3 (10^{-4} M) in CH_2Cl_2[6] has been considered. It shows two evident and large bands at 383 and 257 nm, with the second one probably less intense because it overlaps with different higher energy more intense features. These bands are clearly visible in all the Alq_3 spectra. Two other weaker bands have been found at 333 and 318 nm.[6] These are also present in

TABLE 6: B3LYP/6-31G(d) Singlet−Singlet Excitation Energies and Wavelengths (eV and nm), Oscillator Strengths (*f*), and Composition of the Excited-State Function (Threshold of Reported Coefficients 0.001) for *mer*-Alq_3[a]

excited state	composition[b]	energy (wavelength)	f
2	C-1 → D-1, 0.024		
	C-2 → D-1, 0.102		
	C-3 → D-2, 0.214		
	C-3 → D-3, 0.102		
4	C-1 → D-1, 0.402	2.97 (417)	0.042
	C-2 → D-1, 0.012		
	C-3 → D-2, 0.020		
6	C-2 → D-2, 0.395	3.15 (394)	0.014
	C-2 → D-3, 0.031		
	C-3 → D-2, 0.019		
	C-3 → D-3, 0.014		
10	B-3 → D-3, 0.013	3.97 (313)	0.011
	C-3 → E-1, 0.451		
	C-3 → E-3, 0.015		
11	B-2 → D-1, 0.013	4.08 (304)	0.015
	B-2 → D-2, 0.025		
	B-3 → D-2, 0.017		
	B-3 → D-3, 0.031		
	C-2 → E-1, 0.048		
	C-2 → E-2, 0.038		
	C-3 → E-2, 0.187		
	C-3 → E-3, 0.107		
12	B-1 → D-1, 0.108	4.09 (303)	0.021
	C-1 → E-1, 0.313		
	C-2 → E-1, 0.029		
24	A-γ → D-2, 0.082	4.92 (252)	0.014
	A-γ → D-3, 0.082		
	B-1 → D-1, 0.097		
	B-1 → D-2, 0.119		
	B-1 → D-3, 0.013		
	B-2 → D-2, 0.031		
	B-2 → D-3, 0.019		
25	A-α → D-1, 0.040	4.92 (252)	0.010
	A-β → D-1, 0.080		
	A-β → D-2, 0.015		
	A-γ → D-1, 0.020		
	A-γ → D-3, 0.184		
	B-1 → D-1, 0.036		
	B-1 → D-2, 0.077		
	B-2 → D-3, 0.011		

[a] Only transitions with oscillator strengths higher than 0.01 are reported. The complete list of excitations is reported in the Supporting Information. [b] The molecular orbitals are labeled according to Figure 3.

methyl alcohol solutions and in 50 nm thick amorphous films, but not in the two Alq_3 crystalline forms known as α- and β-phases,[6] in which they are replaced by a shoulder at about 345 nm (a red shift is observed for all the absorptions passing from solution phases to crystal phases).

Table 6 collects computed excitation energies and oscillator strengths up to 251 nm (4.93 eV). Only excitations with oscillator strength equal or larger than 0.010 are reported. The Supporting Information (Table 3S) contains all the computed excitations and details about them. Excited-state compositions are also collected, and allow the grouping of the excitations into different sets. It is possible to distinguish a first set (from excitation 1 to excitation 9) at wavelengths from 447 to 370 nm, a second set (excitations 10−20) from 313 to 262 nm, and a third set (excitations 21−26) from 259 nm to the last computed transition at 251 nm.

The first set of excited states involves excitations from the set C MOs (including the HOMO) into the set D MOs (including the LUMO). The three most intense ones are reported in Table 6. Excitation 2 at 427 nm shows the larger oscillator strength, followed by excitations 4 and 6 at 417 and 394 nm with decreasing oscillator strengths. Excitations 4 and 6 are mainly associated with MOs localized on chelants 1 and 2, respectively, and in this respect they can be considered more localized than excitation 2, which involves the three chelants.

The nodal pattern of orbital D (Figure 4) shows nodes between nitrogen−carbon and carbon−carbon bonds. This pattern appears strongly different from that of orbital C, allowing the prediction of an evident vibronic structure, with consequent lowering and broadening of the absorptions. This vibronic structure should not be associated only with chelant deformations, but it should involve metal−donor bond lengths. In fact, set C MOs have a larger weight on the benzenic ring and oxygen atom of the chelant, while set D MOs principally involve the pyridinic ring and the nitrogen atom. This fact affects metal−donor electrostatic and covalent interactions and presumably leads to the elongation of the Al−O bond and shortening of the Al−N bond in the chelants interested by the excitation. This finding agrees with the CIS/3-21+G** computations of Schlegel and Halls,[20] who computed the first excited-state relaxed geometry and reported similar bond distance percentage deformations (relative to the ground-state geometry) for aluminum−ligand bonds and bonds internal to the ligands. Accordingly, Kushto et al.[21] attributed the observed 700 cm^{-1} spacing in vibronic progression of the argon matrix photoluminescence spectrum to the IR absorption at 651.9 cm^{-1}, assigned to chelant-ring breathing combined with metal−chelant stretching modes.

Different experimental works have pointed out the existence of a strong vibronic structure in low-temperature Alq_3 emission spectra. However, there exists some disagreement about the assignment of the vibronic excitation associated with the maximum of the emission band. Kushto et al. reported a maximum corresponding to the 0 → 5 transition in argon matrix isolation spectra,[21] while Brinkmann et al.[6] reported a maximum corresponding to the 0 → 4 transition and Braun et al.[7] reported a maximum corresponding to the 0 → 3 transition in the α-phase *mer*-Alq_3 crystalline phase.

A vibronic structure with such wide vibronic peak spacing is consistent with the broad first absorption band. However, according to our computation, the presence of three energy-close excited states of significant oscillator strength can also be an important factor to be considered in this regard. Additionally, the computed trend in oscillator strengths of these three excitations reproduces the long tail at higher energies shown in the experimental band. A point to be noted is that these excitations (as all the first nine) are expected to present similarly spaced vibronic progressions as a consequence of the similar shapes (nodal patterns) of sets C and D orbitals on the different chelants.

Another important feature to be considered is that the first excitation shows a significantly lower transition probability relative to the second one (0.005 and 0.067, respectively, as reported in the Supporting Information). This fact might make it difficult to detect the first excitation in absorption spectra. However, in some reported Alq_3 solid-state absorption spectra,[6,25] a small tail in the low-energy region can be observed, suggesting the presence of a low-intensity band overlapped with the successive stronger features. In this regard, it should be noted that the tested pure functionals also predict low oscillator strengths for the first and second excitations (Table 5).

The difference in transition probability between the first and second excitations should be taken into account when *mer*-Alq_3 absorption and emission characteristics are compared. This point

will be thoroughly discussed in the following, when the emission characteristics of *mer*-Alq_3 and *fac*-Alq_3 are considered.

A difference between our findings and the CIS/3-21+G** computations[20] can be underlined. According to the CIS computations, the first excitation involves electronic density changes principally confined to chelant 3 and consequent vibronic relaxation mostly involving the same chelant. According to our computations, the first excitation is dominated by the HOMO−LUMO transition; thus, it mainly consists in charge transfer from chelant 3 to chelant 1. Given the antibond character of orbital D (Figure 4), DFT calculations seem to suggest a relevant geometry deformation of chelant 1 together with a smaller modification of chelant 3.

The second set of excited states (excitations from 10 to 20) involves excitations from set C to set E MOs mixed with excitations from set B to set D MOs. The three more intense excitations in these sets are reported in Table 6. They are excitation 10 at 313 nm (3.97 eV), mainly localized on chelant 3 and essentially involving sets C and E MOs, and excitations 11 and 12 at 303 nm (4.09 eV) and 301 nm (4.11 eV), respectively, which show a larger contribution from sets B and D MOs. These absorptions agree well with the aforementioned experimental weak bands at 333 and 318 nm.

The remaining computed transitions involve excitations from set B to set D orbitals mixed with excitations between sets A and D MOs. The most intense absorptions have been found at 252 nm (4.92 eV), in good agreement with the experimental band at 257 nm.

It should be noted that set A MOs lie very close to lower energy MOs not reported in this work. This fact could give rise to many closely spaced transitions which should be investigated in greater detail for a clear interpretation of this part of the spectrum. Although our study has to be considered a starting analysis of the high-energy excitations, it should also be noted that the highest energy transitions in this paper do not involve high-energy loosely bound virtual MOs. On the contrary, they are associated with excitations to the three most bound virtual MOs (set D MOs).

The lack of transitions to high-energy virtual MOs allows the consideration of the computational results not heavily affected by the wrong asymptotic behavior of the B3LYP xc potential.[10] For the same reason, the addition of diffuse functions should not produce large changes in the computed excitation energies.[10]

We have performed additional computations by using the *mer*-Alq_3 experimental structure obtained from β-phase crystals.[6] In this way we have compared the previously described results associated with the computed geometry with the results associated with the experimental geometry. Small deviations between the two computed spectra (one for the experimental geometry and one for the optimized geometry) would add further likelihood to the previously discussed assignment of the *mer*-Alq_3 experimental features. Furthermore, it would provide a more solid basis for the theoretical comparisons between the two isomers that will be discussed in the following paragraphs. This is of great importance considering the lack of experimental data associated with the *fac*-Alq_3 isomer.

The *mer*-Alq_3 β-phase represents the only crystal structure which has been determined with sufficiently high accuracy for this investigation.[6]

In Table 7, we have reported the energy levels of the MOs close in energy to the HOMO and the LUMO and their shifts relative to the computed geometry (Table 2). This analysis has been restricted to the six highest occupied MOs and the six lowest unoccupied virtual MOs. They represent the orbitals that are pertinent to understand the low-energy absorption and emission properties. It is possible to note that the level scheme retains the structure observed in the case of the computed geometry and that only small changes in the one-electron energies and other characteristics of the MOs are observed. Also in this case, the MOs are substantially localized on the chelants. In fact, the contribution of the central metal is inferior to 1%. Furthermore, they appear principally localized on a single ligand and associated with one fragment orbital. Thus, the MOs have been labeled as described in paragraph 2 regarding the optimized-geometry electronic structure. We can note that orbitals B-3, C-3, D-3, and E-3 (the orbitals principally localized on chelant

TABLE 7: One-Electron Energies of the Six Highest Occupied and the Six Lowest Unoccupied MOs and Their Percentage Composition in Terms of the Aluminum Atom and the Three Quinolin-8-olate Fragments for *mer*-Alq_3 in the Experimental Geometry (β-Phase, Ref 6)[a]

orbital	energy (eV)	composition in terms of fragments (%)
B-1	**−6.96 (0.02)**	Al: 0.0 (0.0) chelant 1: 96.3 (−2.1) chelant 2: 2.6 (+1.8) chelant 3: 1.1 (+0.3)
B-2	**−6.82 (0.02)**	Al: 0.0 (0.0) chelant 1: 2.6 (+1.9) chelant 2: 97.0 (−1.9) chelant 3: 0.4 (0.0)
B-3	**−6.58 (+0.12)**	Al: 0.0 (0.0) chelant 1: 1.0 (+0.2) chelant 2: 0.0 (−0.3) chelant 3: 99.0 (+0.1)
C-1	**−5.29 (+0.04)**	Al: 0.7 (0.0) chelant 1: 87.5 (−8.8) chelant 2: 9.4 (+7.7) chelant 3: 2.4 (+1.1)
C-2	**−5.24 (0.02)**	Al: 0.9 (0.0) chelant 1: 2.1 (+8.7) chelant 2: 85.4 (−1.9) chelant 3: 11.7 (6.8)
C-3 (HOMO)	**−4.89 (+0.11)**	Al: 0.7 (+0.1) chelant 1: 0.6 (+0.1) chelant 2: 5.9 (−6.3) chelant 3: 92.7 (+6.1)
D-1 (LUMO)	**−1.71 (+0.02)**	Al: 0.8 (0.0) chelant 1: 70.5 (−12.8) chelant 2: 28.1 (+12.8) chelant 3: 0.6 (0.0)
D-2	**−1.47 (+0.03)**	Al: 0.5 (0.2) chelant 1: 27.4 (+17.7) chelant 2: 69.7 (+7.1) chelant 3: 2.4 (24.6)
D-3	**−1.35 (+0.17)**	Al: 0.6 (+0.1) chelant 1: 1.7 (−4.8) chelant 2: 1.1 (−20.3) chelant 3: 96.6 (+24.9)
E-1	**−0.48 (+0.07)**	Al: 0.1 (0.0) chelant 1: 82.1 (−9.9) chelant 2: 13.4 (+10.2) chelant 3: 4.3 (−0.3)
E-2	**−0.35 (+0.01)**	Al: 0.1 (0.0) chelant 1: 11.7 (+9.5) chelant 2: 86.4 (−8.9) chelant 3: 1.8 (−0.6)
E-3	**−0.26 (+0.15)**	Al: 0.1 (0.0) chelant 1: 6.1 (+0.4) chelant 2: 0.3 (−1.1) chelant 3: 93.5 (+0.7)

[a] The largest fragment-orbital contributions are reported (threshold 10%). The fragment orbitals are shown in Figure 4. The values in parentheses are the shifts relative to the optimized geometry (reported in Table 2).

TABLE 8: B3LYP/6-31G(d) Singlet−Singlet Excitation Wavelengths (nm) and Oscillator Strengths for *mer*-Alq_3 in the Experimental Geometry (*β*-Phase, Ref 6)[a]

excited state	wave-length	oscillator strength	excited state	wave-length	oscillator strength
1	464 (+17)	0.004 (−0.001)	6	393 (−1)	0.013 (−0.001)
2	429 (+2)	0.038 (−0.029)	7	382 (+3)	0.009 (+0.005)
3	424 (+2)	0.011 (+0.009)	8	360 (−19)	0.007 (+0.001)
4	420 (+3)	0.031 (−0.011)	9	357 (−13)	0.002 (+0.001)
5	412 (+2)	0.020 (+0.019)	10	316 (+3)	0.011 (−0.000)

[a] The values in parentheses are the shifts relative to the optimized geometry parameters collected in Table 6.

3) appear somewhat more localized than the analogous orbitals of the optimized geometry. Furthermore, the same MOs show a larger shift in energy relative to all the other MOs, with more positive energies. As a consequence, there is an increase of the energy gap between the MOs principally localized on chelant 3 and the MOs of the same set principally localized on the other two chelants. Additionally, the HOMO−LUMO gap is reduced to 3.18 eV (0.09 eV lower than that of the optimized geometry).

In Table 8 we report the first 10 excitation wavelengths and relative oscillator strengths computed for the experimental geometry, and their shifts relative to the optimized geometry. These excitations clearly correspond to those reported in Table 6 (optimized geometry), with only small changes regarding their composition. It is possible to note that the first excitation is red-shifted by 17 nm. Excitations from 2 to 7 are not significantly modified, whereas excitations 8 and 9 show blue-shifted wavelengths. Excitation 1 is principally associated with the excitation from the HOMO (C-3) to the LUMO (D-1; see the Supporting Information), and is affected by the reduction of the HOMO−LUMO gap. Thus, it shows a red shift. Excitations 8 and 9 are principally composed of excitations from C-1 and C-2 MOs to the D-3 MO. Since the D-3 MO is shifted toward more positive energies by the geometrical change and C-1 and C-2 do not show a significant shift, these transitions are blue-shifted. Excitations from 2 to 7 principally involve C-1 and C-2 occupied MOs and D-1 and D-2 virtual MOs, whose energies do not change significantly in the experimental geometry. Thus, they do not show any particular change in wavelength. Finally, excitation 10 appears relatively distant from the first nine excitations, as in the case of the optimized geometry.

Although there are small differences between the experimental and theoretical geometries, it is important to note that the general description of the first absorption band remains the same. In particular, the lowest energy excitation (excitation 1) continues to show an oscillator strength substantially inferior to that of excitation 2. Although the oscillator strengths of excitations from 2 to 7 become closer in comparison to the optimized geometry, excitation 2 continues to be the most intense of the first band. Thus, the described attitude of *mer*-Alq_3 to principally absorb radiation through the second and successive excited states remains substantially unchanged.

The differences in the computed electronic structure and absorption spectra between the optimized and experimental geometries are associated with changes of the coordination sphere. In fact, we have performed a further geometry optimization freezing the chelant geometry to the experimental one and optimizing only the geometrical parameters of the coordination sphere (bond distances and bond angles). In this way we have obtained almost the same metal−donor bond distances of the fully optimized geometry and practically the same absorption wavelengths and oscillator strengths.

TABLE 9: B3LYP/6-31G(d) Singlet−Singlet Excitation Energies and Wavelengths (eV and nm), Oscillator Strengths (*f*), and Composition of the Excited Wavefunction (Threshold of Reported Coefficients 0.10) for *fac*-Alq_3[a]

excited state	transition[b]	energy (wavelength)	f
1^1E	C-e → D-e, 0.186	2.89 (429)	0.118
	C-e → D-a, 0.054		
	C-a → D-e, 0.198		
2^1E	C-e → D-e, 0.218	3.00 (414)	0.016
	C-e → D-a, 0.067		
	C-a → D-e, 0.213		
4^1A	B-a → D-a, 0.022	4.01 (309)	0.025
	B-e → D-e, 0.074		
	C-e → E-e, 0.042		
	C-a → E-a, 0.346		
4^1E	B-a → D-e, 0.029	4.02 (308)	0.048
	B-e → D-e, 0.034		
	B-e → D-a, 0.023		
	C-e → E-a, 0.325		
	C-a → E-e, 0.038		
5^1E	B-a → D-e, 0.010	4.20 (295)	0.012
	C-e → E-a, 0.107		
	C-e → E-e, 0.140		
	C-a → E-e, 0.193		
8^1A	B-a → D-a, 0.273	4.81 (258)	0.022
	B-e → D-e, 0.101		
	B-e → D-e, 0.101		

[a] Only electronic excitations with an oscillator strength higher than 0.01 are reported. The complete list of excitations is reported in the Supporting Information. [b] The molecular orbitals are labeled according to Figure 3.

4. Absorption Features of *fac*-Alq_3. The recently discovered Alq_3 crystalline phase attributed to *fac*-Alq_3, called the *δ*-phase, showed photoluminescence excitation spectra with a sharp excitation edge at about 426 nm (2.92 eV).[7] In this spectrum it is not possible to determine any maximum, which should be placed at higher energy.

Table 9 lists the more intense computed transitions up to 257 nm (4.82 eV) for *fac*-Alq_3 (Table 4S in the Supporting Information collects all the computed excitations and other information about them). As for *mer*-Alq_3, the first transitions (from 1^1E to 3^1E) involve electronic excitations from set C orbitals (the HOMO set) to set D orbitals (the LUMO set). However, in this case the first transition (state 1^1E) has the largest oscillator strength. Its calculated excitation energy amounts to 2.89 eV (429 nm), very close to the aforementioned experimental excitation edge at 426 nm.

The *fac*-Alq_3 molecular geometry presents the three oxygen atoms and the three nitrogen atoms in opposite faces of the octahedron, with the dipole moment pointing toward the oxygen atom face. Thus, excitations from set C MOs (more localized on the oxygen atom) to set D MOs (more localized on the nitrogen atom) should be accompanied by a reduction of the dipole moment. Thus, interactions with near molecules should be significantly different in the ground and excited states, probably leading to a larger blue shift. This phenomenon should be taken into account in interpreting experimental deviations from calculations.

As in the case of *mer*-Alq_3, the *fac*-Alq_3 nine lowest energy transitions seem to produce overlapped bands. However, the transitions successive to the first one seem much less intense. This suggests that the first *fac*-Alq_3 band could be sharper than that of the *mer*-Alq_3 analogue.

The first excitation (1^1E) seems to be the most intense among the computed ones, including *mer*-Alq_3 excitations. This represents an important difference when compared to *mer*-Alq_3,

which shows a significantly lower excitation strength for the first excitation. This property is expected to have a relevant effect on the emissive behavior (vide infra).

The transitions from set C to set D MOs cover absorptions from 429 to 398 nm. The next absorption is computed at 309 nm (excited state 4^1A in Table 9). It belongs to a set of absorptions involving transitions between sets C and E MOs mixed with transitions between sets B and D MOs. The most intense excitations are found at 309 nm (4.01 eV, 4^1A), 308 nm (4.02 eV, 4^1E), and 295 nm (4.20 eV, 5^1E). These transitions correspond to those at 313, 304, and 303 nm of *mer*-Alq_3, but their oscillator strengths appear larger.

All the other computed excitations up to 258 nm deal with occupied set B and virtual set D MOs. The most intense absorption within this set seems to be located at 258 nm. It is close to the absorption at 252 nm of *mer*-Alq_3, which principally involves once again the same sets of MOs.

The onset of excitations mainly involving set A MOs is at 257 nm.

5. *fac*-Alq_3 and δ-Phase Crystals. According to the previously discussed computations, the most intense absorption of *fac*-Alq_3 is located at 429 nm (2.89 eV) and corresponds to the lowest energy transition (first excited state). On the other hand, in *mer*-Alq_3 the most intense excitation corresponds to the second excited state at 427 nm (2.90 eV), with the first excitation far less probable (see the Supporting Information for more details). This leads to the prediction of similar locations for the absorption maximum of each isomer. Assuming that δ-phase crystals are constituted by the *fac*-Alq_3 isomer, we can predict similar wavelengths for the lowest energy maximum in the absorption spectra of δ-phase and *mer*-Alq_3 crystals. This implies that the position of this absorption could not be a good property to be used for distinguishing the two isomers. Thus, other spectral properties have to be considered. Possible candidates could be excitation photoluminescence performed on thick samples, fluorescence spectra, and triplet-state population during fluorescence.

Regarding the population of triplet states during fluorescence, a much lower population is reported for δ-phase crystals[7] in comparison to *mer*-Alq_3. A population of 2% has been observed, to be compared with a population of 25% for *mer*-Alq_3 α-phase crystals and amorphous films. The similarity between the *mer*-Alq_3 α-phase and amorphous films suggests that the disorder or molecular packing in condensed phases is not crucial to determine the intersystem crossing toward triplet states or other nonradiative processes. Consequently, the difference in triplet-state population should be interpreted as a property of the single molecule rather than of the whole crystal.

According to our computation, the first transition of *fac*-Alq_3 (1^1E in Table 9) has an oscillator strength much higher than that of the *mer*-Alq_3 first transition (Table 6). This finding suggests a much higher transition probability (transition dipole) between the ground state and the first excited state, but also suggests a much higher emission probability from the first excited state. If we assume that emission takes place from the first excited state in both isomers, we can predict that the radiative process of *fac*-Alq_3 is much faster than that of *mer*-Alq_3. Thus, there is the possibility that nonradiative competitive processes are not as effective in reducing the emission intensity in the case of *fac*-Alq_3 as they are in the case of *mer*-Alq_3. It is important to note that the competition between nonradiative and radiative processes is determined by their relative rates; thus, the preceding discussion needs to be completed by evaluating the rate of nonradiative processes. However, a much faster radiative kinetic constant must be taken into account. In this sense, we can conclude that the presence of *fac*-Alq_3 in δ-phase crystals is consistent with the observed lower triplet-state population during fluorescence.

In the previous discussion, we have assumed that emission takes place from the first excited state in both isomers. This assumption is usual in studies of emission and excited-state dynamics.[26−27] According to the Kasha rule,[28] the radiative decay is almost always significant for the lowest excited singlet state. This property has already been assumed in studies about the luminescence of organic LEDs.[29] In the case of Alq_3 the same hypothesis appears particularly likely by virtue of the closeness in energy between the first nine excited states together with similarities in their chelant-localized character.

The assumption that emission principally involves the first excited state of both isomers leads to a new consideration. As previously discussed, the *mer*-Alq_3 light absorption is expected to be principally determined by transitions to the second and higher excited states by virtue of their larger oscillator strengths when compared to the first excited state. Thus, the excited states interested by absorption are different from the excited state (the first one) involved in the emission, so that the internal conversion toward the first excited state seems to be normally present. This behavior of Alq_3 has been recently proposed as a possible explanation of the experimental time dependence of Alq_3 fluorescence anisotropy.[30] However, considering the results of our computations, a similar phenomenon does not seem to be present in the case of *fac*-Alq_3, where the first excited state should be responsible for both absorption and emission. At this point it seems to be of interest to compare the experimental excited-state dynamics of *mer*-Alq_3 crystals and the δ-phase Alq_3 crystal as a possible way to verify the presence of *fac*-Alq_3 in δ-phase crystals.

The hypothesis that δ-phase Alq_3 contains *fac*-Alq_3 isomer and that emission principally involves the first excited state in both *mer*- and *fac*-Alq_3 explains other differences in excitation photoluminescence and fluorescence emission of the δ-phase crystals and α-phase *mer*-Alq_3. Reported excitation photoluminescence spectra[7] show a sharp excitation edge followed by a plateau, probably due to complete absorption of the incident light, a phenomenon typically observed in large-thickness amorphous films.[24] The presence of the plateau makes it impossible to locate absorption maxima, but these spectra show sharp absorption edges useful in determining the onset of absorption, so that, in the case of thick samples, the high absorbance may allow the assignment of the excitation edge to the first transition. The δ-phase excitation edge is about 1400 cm^{-1} blue-shifted in comparison to that of the *mer*-Alq_3 α-phase (about 22100 cm^{-1} or 452 nm to be compared with about 23500 cm^{-1} or 425 nm). Additionally, low-temperature fluorescence spectra show vibronic structure with spacing of about 550 cm^{-1} in both crystals.[7] Furthermore, the vibronic structure reaches the maximum at the $0 \rightarrow 2$ or $0 \rightarrow 3$ vibronic excitation in both the crystals. However, also in this spectrum, the δ-phase shows blue-shifted emission, with a difference in the $0 \rightarrow 0$ transition of 1600 cm^{-1}, close to the 1400 cm^{-1} blue shift of the excitation edge.

According to the computations, the first excitation in *fac*-Alq_3 is about 940 cm^{-1} blue-shifted relative to that in *mer*-Alq_3. Furthermore, similar vibronic structure spacing and band broadening have to be expected by virtue of the chelant localization of the MOs involved in the excitation and the similarity in the fragment orbitals producing the same MOs (paragraph 2). Consequently, the computations support the

assignment of the blue shifts in excitation absorption and fluorescence spectra as a consequence of higher energy gaps between the first excited state and the ground state for *fac*-Alq_3, and thus are consistent with the presence of this isomer in the crystal.

Conclusions

Computed *mer*-Alq_3 and *fac*-Alq_3 transitions up to about 255 nm (4.93 eV) involve molecular orbitals mainly localized on the chelants. In particular, they involve the six occupied orbitals (sets B and C) and the six virtual orbitals (sets D and E).

The 6-31G(d) basis set, combined with the B3LYP functionals, performed successfully in predicting *mer*-Alq_3 experimental band locations and intensities. Assignment of the absorptions has shown that the first spectral feature (the most important for Alq_3 technological applications) probably is an envelope of absorptions originated by different excited states of similar energy. Given the chelant-localized character of the molecular orbitals involved in the transitions, it has been possible to observe transitions involving the three chelants (the most intense one) and transitions more restricted to a single chelant or a few chelants, while the central metal does not seem to have an important role.

Given the similarity in molecular orbital shapes (nodal pattern) and energy gaps in the two isomers, the *fac*-Alq_3 excitation energies and their assignments are similar to those of *mer*-Alq_3.

According to our computations, the first excitation in *fac*-Alq_3 is 18 nm (940 cm^{-1}) blue-shifted in comparison to that in *mer*-Alq_3. This finding agrees with experimentally observed spectral differences between Alq_3 δ-phase crystals and *mer*-Alq_3 crystals: the 23 nm (1600 cm^{-1}) blue shift in the fluorescence $0 \rightarrow 0$ vibronic transition and the similar blue shift in the excitation edge of the photoluminescence absorption spectra.

The blue-shifted fluorescence and excitation absorption edges observed in Alq_3 δ-phase crystals relative to *mer*-Alq_3 crystals and the lower triplet-state population during fluorescence are experimental findings consistent with emission from the first excited state of the *fac*-Alq_3 isomer. This fact represents a confirmation of the presence of this isomer in δ-phase Alq_3 crystals.

Furthermore, the computations are consistent with emission from the first excited state of *mer*-Alq_3 despite its lower absorption and emission probability than those of the second excited state, which should dominate the first absorption band.

Preliminary tests on the exchange-correlation functional performances have showed that the B3LYP functional is a valuable choice for studying excitations of Alq_3. Comparison of BLYP, BPW91, LB94, and LSDA functionals seems not to leave doubts about its better ability to predict at least the first excitation energies of *mer*-Alq_3. All the pure functionals show too small gaps between occupied and virtual molecular orbitals, and consequent excessively red shifted transitions.

Acknowledgment. M.A. thanks the "consorzio INSTM" for financial support within "Cluster 14 p.e. 5" and for equipment within the "Cluster 26 p.e. 8" fellowship.

Supporting Information Available: Table 1S containing the *fac*-Alq_3 Cartesian coordinates optimized at the B3LYP/3-21G* and B3LYP/6-31G* levels of approximation, Table 2S containing the analogue coordinates for *mer*-Alq_3, and Tables 3S and 4S listing information about all the computed electronic absorptions of *mer*-Alq_3 and *fac*-Alq_3 (in this case the B3LYP/6-31G* level of approximation has been used in TD-DFT computations; excitation energies, oscillator strengths, and excited-state composition have been reported for each computed excited state). This material is available free of charge via the Internet at http://pubs.acs.org.

References and Notes

(1) Condren, S. M.; Lisensky, G. C.; Ellis, A. B.; Nordell, K. J.; Kuech, T. F.; Stockman, S. A. *J. Chem. Educ.* **2001**, *78*, 1033.
(2) Curioni, A.; Boero, M.; Andreoni, W. *Chem. Phys. Lett.* **1998**, *294*, 263.
(3) Schmidbaur, H.; Lettenbauer, J.; Wilkinson, D. L.; Müller, G.; Kumberger, O. *Z. Naturforsch., B* **1991**, *46*, 901.
(4) Fujii, I.; Hirayama, N.; Ohtani, J.; Kodama, K. *Anal. Sci.* **1996**, *12*, 153.
(5) Baker, B. C.; Sawyer, D. T. *Anal. Chem.* **1968**, *40*, 1945.
(6) Brinkmann, M.; Gadret, G.; Muccini, M.; Taliani, C.; Masciocchi, N.; Sironi, A. *J. Am. Chem. Soc.* **2000**, *122*, 5147.
(7) Braun, M.; Gmeiner, J.; Tzolov, M.; Coelle, M.; Meyer, F. D.; Milius, W.; Hillebrecht H.; Wendland, O.; von Schütz, J. U.; Brutting, W. *J. Chem. Phys.* **2001**, *114*, 9625.
(8) Becke, A. D. *J. Chem. Phys.* **1993**, *98*, 5648.
(9) Casida, M. Time dependent density functional response theory for molecules. In *Recent Advances in Density Functional Methods*; Chong, D. P., Ed.; World Scientific: Singapore, 1995; Vol. 1, p 155.
(10) Casida, M. E.; Jamorski, C.; Casida, K. C.; Salahub, D. R. *J. Chem. Phys.* **1998**, *108*, 4439.
(11) Becke, A. D. *Phys. Rev. A* **1988**, *38*, 3098.
(12) Lee, C.; Yang, W.; Parr, R. G. *Phys. Rev. B* **1988**, *37*, 785.
(13) Perdew, J. P.; Chevary, J. A.; Vosko, S. H.; Jackson, K. A.; Pederson, M. R.; Singh, D. J.; Fiolhais, C. *Phys. Rev. B* **1992**, *46*, 6671.
(14) Vosko, S. H.; Wilk, L.; Nusair, M. *Can. J. Phys.* **1980**, *58*, 1200.
(15) Van Leeuwen, R.; Baerends, E. J. *Phys. Rev. A* **1994**, *49*, 2421.
(16) Frisch, M. J.; Trucks, G. W.; Schlegel, H. B.; Scuseria, G. E.; Robb, M. A.; Cheeseman, J. R.; Zakrzewski, V. G.; Montgomery, J. A., Jr.; Stratmann, R. E.; Burant, J. C.; Dapprich, S.; Millam, J. M.; Daniels, A. D.; Kudin, K. N.; Strain, M. C.; Farkas, O.; Tomasi, J.; Barone, V.; Cossi, M.; Cammi, R.; Mennucci, B.; Pomelli, C.; Adamo, C.; Clifford, S.; Ochterski, J.; Petersson, G. A.; Ayala, P. Y.; Cui, Q.; Morokuma, K.; Malick, D. K.; Rabuck, A. D.; Raghavachari, K.; Foresman, J. B.; Cioslowski, J.; Ortiz, J. V.; Stefanov, B. B.; Liu, G.; Liashenko, A.; Piskorz, P.; Komaromi, I.; Gomperts, R.; Martin, R. L.; Fox, D. J.; Keith, T.; Al-Laham, M. A.; Peng, C. Y.; Nanayakkara, A.; Gonzalez, C.; Challacombe, M.; Gill, P. M. W.; Johnson, B. G.; Chen, W.; Wong, M. W.; Andres, J. L.; Head-Gordon, M.; Replogle, E. S.; Pople, J. A. *Gaussian 98*, revision A.11; Gaussian, Inc.: Pittsburgh, PA, 2001.
(17) Fonseca Guerra, C.; Visser, O.; Snijders, J. G.; te Velde, G.; Baerends, E. J. Parallelisation of the Amsterdam Density Functional Program. In *Methods and Techniques for Computational Chemistry*; Clementi, E., Corongiu, G., Eds.; STEF: Cagliari, Italy, 1995; pp 305−395.
(18) Available at http://tc.chem.vu.nl/SCM/Doc/atomicdatabase.
(19) Schaftenaar, G.; Noordik, J. H. *J. Comput.-Aided Mol. Des.* **2000**, *14*, 123 (www.cmbi.kun.nl/~schaft/molden/molden.html).
(20) Halls, M. D.; Schlegel, H. B. *Chem. Mater.* **2001**, *13*, 2632.
(21) Kushto, G. P.; Iizumi, Y.; Kido, J.; Kafafi, Z. H. *J. Phys. Chem. A* **2000**, *104*, 3670.
(22) Anderson, J. D.; McDonald, E. M.; Lee, P. A.; Anderson, M. L.; Ritchie, E. L.; Hall, H. K.; Hopkins, T.; Mash, E. A.; Wang, J.; Padias, A.; Thayumanavan, S.; Barlow, S.; Marder, S. R.; Jabbour, G. E.; Shaheen, S.; Kippelen, B.; Peyghambarian, N.; Wightman, R. M.; Armstrong, N. R. *J. Am. Chem. Soc.* **1998**, *120*, 9646.
(23) Hopkins, T. A.; Meerholz, K.; Shaheen, S.; Anderson, M. L.; Schimdt, A.; Kippelen, B.; Padias, A. B.; Hall, H. K.; Peyghambarian, N., Jr.; Armstrong, N. R. *Chem. Mater.* **1996**, *8*, 344.
(24) Garbuzov, D. Z.; Bulovic, V.; Burrows, P. E.; Forrest, S. R. *Chem. Phys. Lett.* **1996**, *249*, 433.
(25) Martin, R. L.; Kress, J. D.; Campbell, I. H.; Smith, D. L. *Phys. Rev. B* **2000**, *61*, 15804.
(26) Hameka, H. F. In *Triplet Decay and Intersystem Crossing in Aromatic Hydrocarbons*; Zahlan, A. B., Androes, G. M., Hameka, H. F., Heineken F. M., Hutchison, C. A., Jr., Robinson, G. W., van der Waals, J. H., Eds.; Cambridge University Press: Cambridge, 1967.
(27) Birks, J. B. *Photophysics of Aromatic Molecules*; Wiley-Interscience: London, 1970.
(28) Kasha, M. *Discuss. Faraday Soc.* **1950**, *9*, 14.
(29) Burin, A. L.; Ratner M. A. *J. Chem. Phys.* **1998**, *109*, 6092.
(30) van Veldhoven, E.; Zhang, H.; Glasbeek, M. *J. Phys. Chem. A* **2001**, *105*, 1687.